

Spiral arms in CALIFA galaxies traced by non-circular velocities, abundances, and extinctions

F. Sakhibov¹, I. A. Zinchenko^{2,3}, L. S. Piluygin^{2,3}, E. K. Grebel³, A. Just³, J. M. Vílchez⁴

¹ *University of Applied Sciences of Mittelhessen, Campus Friedberg, Department of Mathematics, Natural Sciences and Data Processing, Wilhelm-Leuschner-Straße 13, 61169 Friedberg, Germany*

² *Main Astronomical Observatory of National Academy of Sciences of Ukraine, 27 Zabolotnogo str., 03680 Kiev, Ukraine*

³ *Astronomisches Rechen-Institut, Zentrum für Astronomie der Universität Heidelberg, Mönchhofstr. 12–14, 69120 Heidelberg, Germany*

⁴ *Instituto de Astrofísica de Andalucía, CSIC, Apdo, 3004, 18080 Granada, Spain*

Accepted 2017 Month 00. Received 2017 Month 00; in original form 2017 March 09

ABSTRACT

We derive maps of the observed velocity of ionized gas, the oxygen abundance, and the extinction (Balmer decrement) across the area of the four spiral galaxies NGC 36, NGC 180, NGC 6063, and NGC 7653 from integral field spectroscopy obtained by the Calar Alto Legacy Integral Field Area (CALIFA) survey. We searched for spiral arms through Fourier analysis of the spatial distribution of three tracers (non-circular motion, enhancement of the oxygen abundance, and of the extinction) in the discs of our target galaxies. The spiral arms (two-armed logarithmic spirals in the deprojected map) are shown in each target galaxy for each tracer considered. The pitch angles of the spiral arms in a given galaxy obtained with the three different tracers are close to each other. The enhancement of the oxygen abundance in the spiral arms as compared to the abundance in the interarm regions at a given galactocentric distance is small; within a few per cent. We identified a metallicity gradient in our target galaxies. Both barred galaxies in our sample show flatter gradients than the two galaxies without bars. Galactic inclination, position angle of the major axis, and the rotation curve were also obtained for each target galaxy using the Fourier analysis of the two-dimensional velocity map.

Key words: H II regions – galaxies: spectroscopy – galaxies: ISM – galaxies

1 INTRODUCTION

Spiral arms are a prominent feature of late-type regular disc galaxies. The spirals arms in galaxies have been investigated via the analysis of the spatial distribution of different tracers such as the positions of H II regions (e.g., Kalnajs 1975; Considere & Athanasoulas 1982), the light distribution at a given wavelength (e.g., Iye et al. 1982; Elmegreen & Elmegreen 1984; Considere & Athanasoulas 1988; Eskridge et al. 2002), the velocity of gas clouds (e.g., Rots 1975; Sakhibov & Smirnov 1987, 1989, 1990, 2004; Canzian 1993; Fridman et al. 2001a,b), the dust distribution (e.g., Grosbol et al. 1999), magnetic fields (e.g., Vallée 1995; Frick et al. 2016), etc.

The investigation of spiral arms requires a detailed map of the chosen tracers across the galactic disc. Spiral arms appear as a deviation from the axisymmetric distribution of the tracer (e.g., velocity, abundance, etc.). Since the amplitude of the deviation is small, high-quality measurements of the tracer are required in order to reveal the spiral arm. Integral field spectroscopy of galaxies provides information about the spatial distribution of different tracers simultaneously and allows us to compare between parameters of the spiral arms determined through different tracers. This is par-

ticularly useful when examining the link between the kinematical and other properties of spiral arms.

Observations with integral field spectroscopy were carried out for a large sample of galaxies in the framework of the “Calar Alto Legacy Integral Field Area Survey” (CALIFA, see Sánchez et al. 2012a; Husemann et al. 2013; García-Benito et al. 2015). These data have enabled studies of the radial and azimuthal distributions of different characteristics in galaxies such as their stellar populations (Sánchez-Blázquez et al. 2014; Martín-Navarro et al. 2015), star formation rate and history (Pérez et al. 2013; González Delgado et al. 2014, 2016), motions of the ionized gas (Barrera-Ballesteros et al. 2015; García-Lorenzo et al. 2015; Holmes et al. 2015), and oxygen abundances (Sánchez et al. 2012b; Piluygin et al. 2014; Sánchez et al. 2014; Zinchenko et al. 2016; Sánchez-Menguiano et al. 2016a).

In our current study we will construct maps of the velocity field of the ionized gas, of oxygen abundances, and of the extinction (Balmer decrement) within the optical radius, R_{25} , in the discs of four galaxies with two-dimensional spectroscopy from the CALIFA survey. We will search for the manifestation of spiral arms using the method of Fourier analysis of the azimuthal distribution of the tracers (non-circular motions, oxygen abundance, and ex-

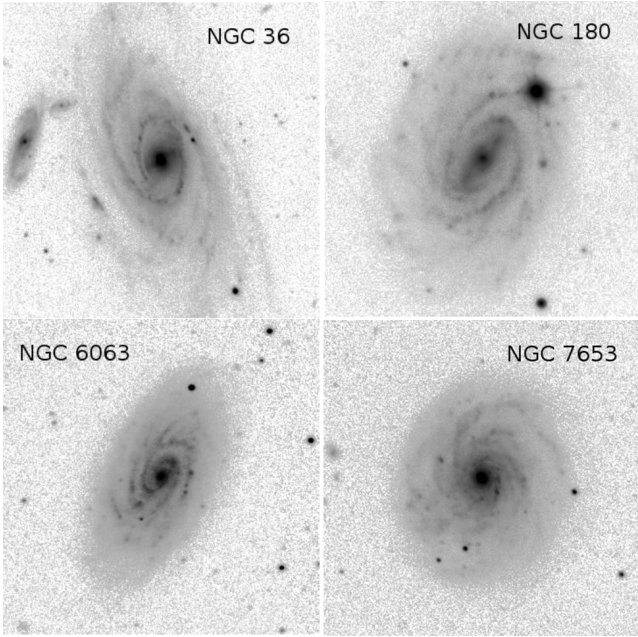


Figure 1. Images of the target galaxies are shown in the Sloan Digital Sky Survey (SDSS) g filter (4686Å). The images are taken from the NASA Extragalactic Database (NED). North is up and east is to the left.

tion) in thin ring zones at different galactocentric distances in the plane of the galaxy. The decomposition of the two-dimensional maps of different tracers through Fourier analysis allows us to quantify structures in a range of scales from $\sim 0.2R_{25}$ to $\sim 0.7R_{25}$. The Fourier analysis provides data on the multiplicity (simultaneous existence of several modes), geometrical form, and radial extent of the spiral arms. Such an analysis was used before to determine the spiral arms from the positions of H II regions (Considere & Athanassoula 1982), the light distribution at a given wavelength (Considere & Athanassoula 1988), and velocity fields of ionized gas (Sakhibov & Smirnov 1987, 1989, 1990, 2004; Canzian 1993; Fridman et al. 2001a,b). Our aim is to determine the parameters of the spiral arms based on different tracers, and to study their morphological relations.

The paper is structured as follows. The data are discussed in Section 2. In Section 3 we describe the method of the Fourier analysis of a two-dimensional velocity field and the results obtained for our target galaxies. The determination of the spiral arms from the oxygen abundance and the extinction maps is described in Section 4. The comparison between spiral arms derived from different tracers is given in Section 5. Section 6 summarizes our conclusions.

2 THE DATA

We selected four galaxies from the sample of CALIFA galaxies studied in Zinchenko et al. (2016). We chose galaxies where the spaxels with measured emission lines are homogeneously distributed over the image of the galaxy. Images of the target galaxies in the Sloan Digital Sky Survey (SDSS) g filter are shown in Fig. 1. The images are taken from the NASA Extragalactic Database (NED)¹. The processing of the observational data is re-

ported in Zinchenko et al. (2016). Therefore we just briefly describe the data analysis steps and report additional measurements performed here.

We used publicly available spectra from the CALIFA survey data release 2 (DR2; Sánchez et al. (2012a); García-Benito et al. (2015); Walcher et al. (2014)), based on observations with the PMAS/PPAK integral field spectrophotometer mounted on the Calar Alto 3.5-m telescope in Spain. We used the low-resolution data cubes (setup V500) to determine the spatial distribution of the physical parameters of the interstellar ionized gas. The integrated stellar spectra in all spaxels were fitted using the public version of the STARLIGHT code (Cid Fernandes et al. 2005; Mateus et al. 2006; Asari et al. 2007) adapted for execution in the NorduGrid ARC² environment of the Ukrainian National Grid. We used a set of 45 synthetic simple stellar population (SSP) spectra with metallicities $Z = 0.004, 0.02$, and 0.05 , and 15 ages from 1 Myr up to 13 Gyr from the evolutionary synthesis models of Bruzual & Charlot (2003), and the reddening law of Cardelli et al. (1989) with $R_V = 3.1$. The nebular emission spectrum in each spaxel was obtained by subtracting the stellar population synthesis spectrum from the observed one. The profiles of H β , H α , [OIII] $\lambda\lambda 4959, 5007$, [NII] $\lambda\lambda 6548, 6584$, and [SII] $\lambda\lambda 6717, 6731$ lines were fitted by Gaussians.

The line-of-sight velocity of the interstellar gas was determined from the wavelength of the centre of the H α line profile. The observed velocity fields of the target galaxies corrected for the systemic velocity of each galaxy, V_{sys} , are shown in Fig. 2. We list the inferred values of V_{sys} in Table 3.

The measured line fluxes were corrected for interstellar reddening using the theoretical H α to H β ratio from Osterbrock (1989), assuming case B recombination, an electron temperature of 10,000 K, and the analytical approximation to the Whitford interstellar reddening law by Izotov et al. (1994). If the measured value of the ratio H α /H β is lower than the theoretical one (2.86) then the reddening is adopted to be zero.

We used the oxygen abundances determined in Zinchenko et al. (2016) through a strong-line method (the C method, Pilyugin et al. 2012). It should be noted that the C method produces oxygen abundances compatible to the metallicity scale defined by H II regions with T_e -based abundances.

For the further analysis of the velocity field and the extinction map we selected spaxels with a ratio of the flux to the flux error $\epsilon \geq 8$ for the H α emission line. For the oxygen abundance map, only spaxels with $\epsilon \geq 3$ for each of the H β , H α , [OIII] $\lambda 5007$, [NII] $\lambda 6584$ lines were selected for further analysis.

The properties of our target galaxies are given in Table 1. The galaxy name is reported in the first column. The morphological type and the morphological type code T of the galaxy taken from the LEDA data base³ (Paturel et al. 2003) are reported in Columns 2 and 3. The stellar mass of the galaxy and its absolute magnitude are listed in Columns 4 and 5. The galaxy inclination and position angle of the major axis obtained from the analysis of the photometric map are reported in Columns 6 and 7. The isophotal radii R_{25} in arcmin and in kpc are given in Columns 8 and 9, respectively. The adopted distance is listed in Column 10.

Our subsequent study is based on the maps of velocity, oxygen abundance, and extinction A_V (Balmer decrement) of the four galaxies.

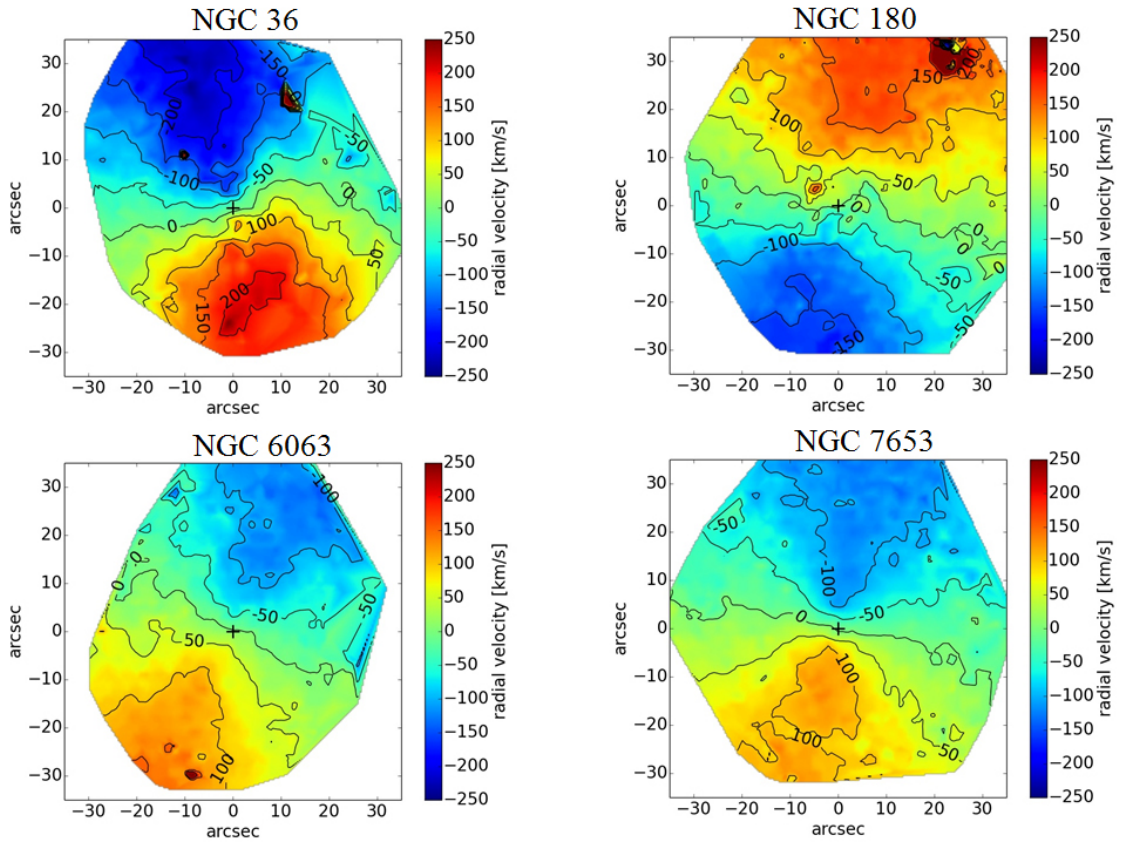
¹ <https://ned.ipac.caltech.edu/>

² <http://www.nordugrid.org/>

³ <http://leda.univ-lyon1.fr/>

Table 1. The galaxy sample.

Galaxy	Type	T-type	$\log(M_*)^a$	M_R^b [mag]	Inclination ^c [degree]	PA ^c [degree]	R_{25}^c [arcmin]	R_{25}^c [kpc]	V_{max}^d [km s ⁻¹]	D [Mpc]
1	2	3	4	5	6	7	8	9	10	11
NGC 36	SABb	3.0	10.82	-22.34	64	14	0.95	22.38	253.8	81.0
NGC 180	Sc	4.6	10.66	-22.27	46	165	1.09	22.39	217	70.6
NGC 6063	Scd	5.9	9.94	-20.54	56	156	0.75	10.19	141.6	46.7
NGC 7653	Sb	3.1	10.48	-21.62	31	175	0.77	13.06	228	58.3

^a Stellar mass estimated by the CALIFA collaboration (Walcher et al. 2014)^b R-band absolute magnitude obtained by the CALIFA collaboration (Walcher et al. 2014)^c Values taken from Zinchenko et al. (2016)^d Maximum rotation velocity corrected for inclination (<http://leda.univ-lyon1.fr/search.html>)**Figure 2.** The colour-coded maps of the observed velocity fields in the target galaxies corrected for the systemic velocity of the respective galaxy as a whole. The lines show the contours of equal line-of-sight velocities. The contours are separated by 50 km s⁻¹. The position of the centre of the galaxy is marked by a plus sign.

3 THE KINEMATIC SPIRAL ARMS

3.1 Fourier coefficients from the velocity field

The Fourier transformation method is used to decompose a two-dimensional velocity field into a hierarchy of structures on different scales. This method, applied to a number of narrow concentric annuli in radial direction of the galaxy, allows one to extract the field of perturbations in both the angular and radial components of the velocity and to investigate logarithmic and other types of spiral arms. It should be noted that there is no assumption of the shape of the spiral arms with this method. In the current Section this method

is applied to the two-dimensional velocity fields to investigate the spiral structure of the velocity perturbations arising due to spiral density waves.

The line-of-sight velocity field of the gas in galactic discs exhibits deviations from a purely circular motion, which are associated with the spiral arms of the galaxy (Visser 1980). These deviations could be due to the influence of a spiral density wave on the circular rotation of the gas in the disc (Lin et al. 1969). The tangential and radial components of perturbed velocities (δV_θ , δV_R) caused by a spiral density wave depend on the amplitude of the wave, the position of the corotation and Lindblad resonances, and

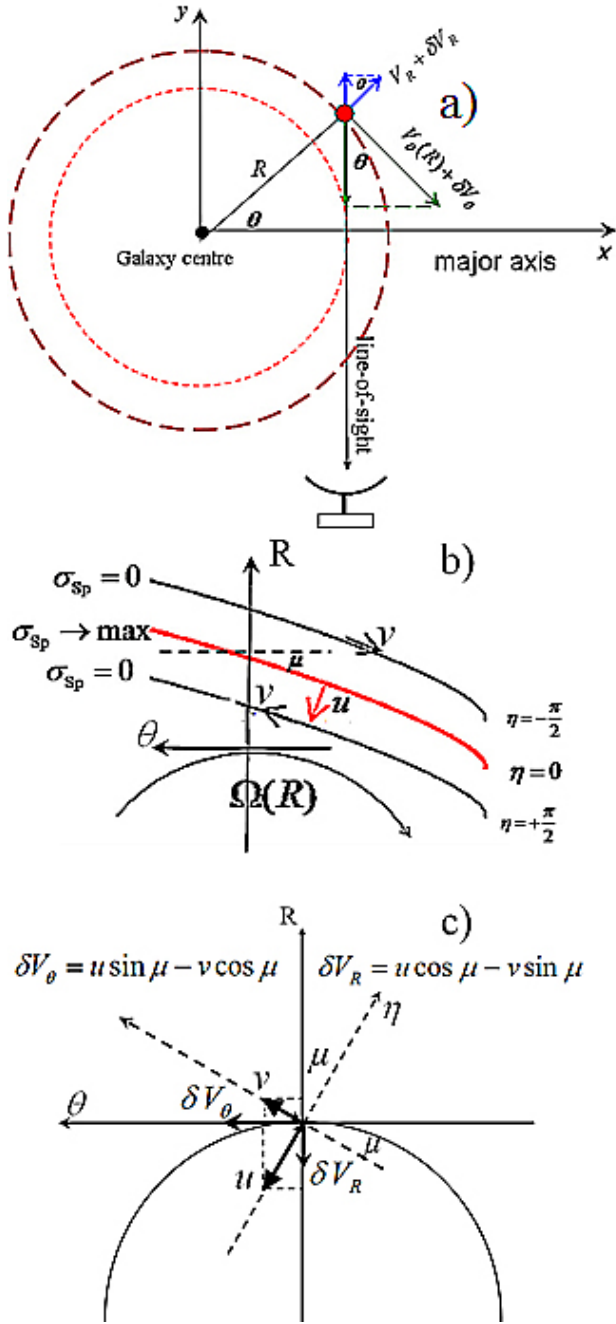


Figure 3. *a)* Contributions of the different components of the gas motion to the line-of-sight velocity. *b)* The velocity field of a spiral density wave. σ_{sp} denotes the density perturbation of the galactic disc. The pitch angle of the spiral arm, μ , is defined as the angle between tangents to the circle and to the spiral arm. The lines of equal spiral arm phase, $\eta = \text{const}$, are lines of equal density and velocity perturbation. The component of the streaming velocity perpendicular to the spiral arm, u , has its extreme value at $\eta = 0$. The tangential streaming velocity, v , reaches its extreme values for $\eta = \pm\pi/2$, i.e., at the outer and inner spiral arm borders (perturbed density $\sigma_{sp} = 0$). *c)* The radial (along the direction of increasing galactocentric distance) and tangential (parallel to the direction of rotation) components of the velocity perturbations (δV_R , δV_θ) are related to the streaming velocity (u , v) by Eq. 5 and depend on the pitch angle μ .

the mass distribution within the galaxy. Here R is the deprojected galactocentric distance in the plane of the galaxy and θ is the polar angle, measured from the major axis of the galaxy. There can also be deviations from pure circular motions of other types, e.g., a radially symmetric outflow or inflow toward the center of the galaxy, caused by bars, warps, lopsidedness, or a galactic fountain (e.g., Bosma 1978; Sakhibov & Smirnov 1987, 1989, 1990, 2004; Fraternali et al. 2001; Schinnerer et al. 2000). The description of different approaches to the modelling of non-circular motions in a two-dimensional velocity map is given in Spekkens & Sellwood (2007), where the non-circular motions with rather high velocities due to a bar-like distortion of an axisymmetric potential are considered. The objective of the present paper is to examine the non-circular motions caused by density wave perturbations. It is expected that the radial velocities caused by a bar can exceed the non-circular velocities caused by density wave perturbations in the bar region. We will investigate the non-circular motions in the disc outside the bars where radial velocities caused by the spiral perturbation are expected to make a dominant contribution to the non-circular motions.

The contributions of the perturbed tangential (δV_θ) and radial (δV_R) components of the velocity to the observed line-of-sight velocity are given by the equation (see Fig. 3a)

$$V_{sp} = \left(\delta V_\theta(R, \theta) \cdot \cos \theta + \delta V_R(R, \theta) \cdot \sin \theta \right) \cdot \sin i \quad (1)$$

Thus, the line-of-sight velocity $V_r^{obs}(R, \theta)$ observed at a given point of the disc involves the velocity of the galaxy as a whole, V_{gal} , the rotation velocity, $V_\theta(R)$, a pure radial inflow or outflow V_R , and the velocities δV_θ and δV_R caused by the density wave perturbation (see Fig. 3a).

$$\frac{V_r^{obs}(R, \theta)}{\sin i} = V_{gal} + \left(V_\theta(R) + \delta V_\theta(R, \theta) \right) \cdot \cos \theta + \left(V_R + \delta V_R(R, \theta) \right) \cdot \sin \theta \quad (2)$$

where i is the inclination angle of the galaxy.

Our aim is to extract the contributions caused by the spiral density wave, δV_θ and δV_R , to the observed velocity $V_r^{obs}(R, \theta)$. If the gravitational potential of a disc galaxy is perturbed by a rotating spiral wave, the gas in the disc reacts by streaming motions that are also of spiral shape. The response of the gas then is

$$\begin{aligned} u &= \hat{u} \cos \eta \\ v &= -\hat{v} \sin \eta \end{aligned} \quad (3)$$

where η is the phase of the perturbation by a spiral wave (which varies across the spiral arm, see Fig. 3b)

$$\eta = -m\theta + mh \cot \mu \ln(R/R_0) \quad (4)$$

where $h = +1$ and $h = -1$ for an S- and Z-spiral arm, respectively, μ is the pitch angle (a measurement of the tightness of the winding of spiral arms), and m is the number of the arms. The parameter h determines the direction of winding of the spiral arm in the sky: S-shaped or Z-shaped. Note that a right-handed coordinate system is used. The values \hat{u} and \hat{v} are amplitudes (extreme values) of orthogonal (across the spiral arm) and tangential streaming velocities. The orthogonal streaming velocity has its extreme value at the centre of the spiral arm for $\eta = 0$ and the tangential streaming velocity has its extreme values at the outer and inner spiral arm borders for $\eta = \pm\pi/2$ (Fig. 3b).

The orthogonal and tangential streaming velocities make a contribution to the observed line-of-sight velocity $V_r^{obs}(R, \theta)$ in the form of the velocity perturbations (δV_R , δV_θ). The radial (along the

direction of increasing galactocentric distance) and tangential (parallel to the direction of rotation) components of the velocity perturbations (δV_R , δV_θ) are related to the streaming velocity (u , v) by Eq. 5 and depend on the geometrical form (pitch angle μ) of the spiral arm (see Fig. 3c)

$$\begin{aligned}\delta V_\theta &= h(u \sin \mu - v \cos \mu) \\ \delta V_R &= u \cos \mu - v \sin \mu\end{aligned}\quad (5)$$

Using Eq. (3) to Eq. (5) and grouping the sine and cosine terms of identical quantities of θ , the perturbed motion V_{sp} (Eq. (1)) caused by the mode m can be written in the form

$$\begin{aligned}V_{sp} &= \frac{1}{2}(\hat{u} - \hat{v}) \cdot \cos((m-1)\theta) \cdot \sin(m \cot \mu \ln(R/R_0) + \mu) \\ &\quad - \frac{1}{2}(\hat{u} - \hat{v}) \cdot \sin((m-1)\theta) \cdot \cos(m \cot \mu \ln(R/R_0) + \mu) \\ &\quad - \frac{1}{2}(\hat{u} + \hat{v}) \cdot \cos((m+1)\theta) \cdot \sin(m \cot \mu \ln(R/R_0) - \mu) \\ &\quad + \frac{1}{2}(\hat{u} + \hat{v}) \cdot \sin((m+1)\theta) \cdot \cos(m \cot \mu \ln(R/R_0) - \mu)\end{aligned}\quad (6)$$

Eq. (6) corresponds the case of $h = +1$, because all our target galaxies are S-spirals. The coefficients of the sines and cosines of the polar angles $(m-1)\theta$ and $(m+1)\theta$ determine the contribution of the velocity perturbations to the observed line-of-sight velocity. Inspection of Eq. (6) shows that the second mode of the spiral-density wave ($m = 2$) – a two-armed spiral – contributes to the values multiplied by the sines and cosines of the polar angles θ and 3θ while the first mode ($m = 1$) – a one-armed spiral – contributes to the values multiplied by the sines and cosines of the polar angles $\theta = 0$ and 2θ .

Eq. (6) and Eq. (2) result in

$$\begin{aligned}\frac{V_r^{obs}(R, \theta)}{\sin i} &= a_0 + a_1 \cos(\theta) + b_1 \sin(\theta) + \\ &\quad + a_2 \cos(2\theta) + b_2 \sin(2\theta) + a_3 \cos(3\theta) + b_3 \sin(3\theta)\end{aligned}\quad (7)$$

where the coefficients $a_0, a_1, b_1, a_2, b_2, a_3$, and b_3 are

$$\begin{aligned}a_0 &= V_{gal} + \frac{1}{2}(\hat{u}_1 - \hat{v}_1) \cdot \sin(\cot \mu_1 \ln(R/R_{01}) + \mu_1) \\ a_1 &= V_\theta(R) + \frac{1}{2}(\hat{u}_2 - \hat{v}_2) \cdot \sin(2 \cot \mu_2 \ln(R/R_{02}) + \mu_2) \\ b_1 &= V_R - \frac{1}{2}(\hat{u}_2 - \hat{v}_2) \cdot \cos(2 \cot \mu_2 \ln(R/R_{02}) + \mu_2) \\ a_2 &= -\frac{1}{2}(\hat{u}_1 + \hat{v}_1) \cdot \sin(\cot \mu_1 \ln(R/R_{01}) - \mu_1) \\ b_2 &= \frac{1}{2}(\hat{u}_1 + \hat{v}_1) \cdot \cos(\cot \mu_1 \ln(R/R_{01}) - \mu_1) \\ a_3 &= -\frac{1}{2}(\hat{u}_2 + \hat{v}_2) \cdot \sin(2 \cot \mu_2 \ln(R/R_{02}) - \mu_2) \\ b_3 &= \frac{1}{2}(\hat{u}_2 + \hat{v}_2) \cdot \cos(2 \cot \mu_2 \ln(R/R_{02}) - \mu_2)\end{aligned}\quad (8)$$

Hereafter the quantities \hat{u}_1 , \hat{v}_1 , μ_1 , and R_{01} mean the velocity perturbation amplitudes, the pitch angle, and scaling factor for the first mode ($m = 1$), and \hat{u}_2 , \hat{v}_2 , μ_2 , and R_{02} stand for the velocity perturbation amplitudes, the pitch angle, and the scaling factor for the second mode ($m = 2$) of a spiral density wave, respectively.

The systemic velocity V_{gal} of the galaxy (not corrected for inclination) contributes in the zeroth Fourier harmonic and mixes with the velocity perturbation from the first mode $m = 1$ of the spiral density wave.

The circular rotation $V_\theta(R)$ contributes in the first Fourier harmonics (a_1) and mixes with the velocity perturbation from the second mode $m = 2$ of the spiral density wave.

The first mode of the spiral wave ($m = 1$) – a one-armed asymmetric structure – contributes to the zeroth and second Fourier harmonics of the azimuthal distribution of the observed line-of-sight velocities. The second mode of the spiral-density wave ($m = 2$) – a two-armed spiral – contributes also to the first and third Fourier harmonics of the azimuthal distribution of line-of-sight velocities at a given galactocentric distance, R . Since the zeroth Fourier coefficient, a_0 , may include a contribution not only from the systemic velocity of the galaxy V_{gal} but also from the first mode of the spiral density wave, the zeroth Fourier coefficient must change in radial direction along the galactic disc.

Thus, if the velocity of the galaxy, V_{gal} , and the radial change of the Fourier coefficients, $a_1(R)$, are determined, the pure rotation curve of the galaxy, $V_\theta(R)$, can be measured. The radial variation of the coefficients $a_2(R)$, $b_2(R)$, $a_3(R)$, and $b_3(R)$ defines the amplitude of the velocity perturbations caused by the spiral arms as well as the geometric form of the arms. Thus, the problem of the analysis of the residual velocities caused by a spiral density wave can be reduced to the determination of the first three harmonics of the Fourier series of the observed azimuthal distribution of the line-of-sight velocities for the thin ring zones.

There is also an impact of the bar in the inner part of a barred galaxy. Accounting for the impact of the bar, according to the bisymmetric model by Spekkens & Sellwood (2007), changes Eq. 2 for the observed line-of-sight velocity:

$$\begin{aligned}\frac{V_r^{obs}(R, \theta)}{\sin i} &= V_{gal} + \left(V_\theta(R) + \delta V_\theta(R, \theta) + V_{2,t} \right) \cdot \cos \theta + \\ &\quad + \left(V_R + \delta V_R(R, \theta) + V_{2,r} \right) \cdot \sin \theta\end{aligned}\quad (9)$$

where $V_{2,t} = \hat{V}_{2,t} \cos(2\theta_b)$ and $V_{2,r} = \hat{V}_{2,r} \sin(2\theta_b)$ are the tangential and radial components of the non-circular flow caused by the bar. These components vary with the angle to the bar axis $\theta_b = \theta - \phi_b$ as the cosine and sine of $2\theta_b$, respectively. The major axis of the bar lies at an angle ϕ_b to the projected major axis of the galaxy (see Fig. 1 in Spekkens & Sellwood (2007)). The maximal amplitudes of the tangential and radial components of the non-circular flow caused by bar, $\hat{V}_{2,t}(R)$ and $\hat{V}_{2,r}(R)$, respectively, are both functions of the radius. Eq. 8 can be rewritten as:

$$\begin{aligned}a_0 &= V_{gal} + \frac{1}{2}(\hat{u}_1 - \hat{v}_1) \cdot \sin(\cot \mu_1 \ln(R/R_{01}) + \mu_1) \\ a_1 &= V_\theta(R) + \frac{1}{2}(\hat{u}_2 - \hat{v}_2) \cdot \sin(2\theta_{sp2} + \mu_2) - \frac{1}{2}(\hat{V}_{2,t} - \hat{V}_{2,r}) \cdot \sin(2\phi_b) \\ b_1 &= V_R - \frac{1}{2}(\hat{u}_2 - \hat{v}_2) \cdot \cos(2\theta_{sp2} + \mu_2) + \frac{1}{2}(\hat{V}_{2,t} - \hat{V}_{2,r}) \cdot \cos(2\phi_b) \\ a_2 &= -\frac{1}{2}(\hat{u}_1 + \hat{v}_1) \cdot \sin(\cot \mu_1 \ln(R/R_{01}) - \mu_1) \\ b_2 &= \frac{1}{2}(\hat{u}_1 + \hat{v}_1) \cdot \cos(\cot \mu_1 \ln(R/R_{01}) - \mu_1) \\ a_3 &= -\frac{1}{2}(\hat{u}_2 + \hat{v}_2) \cdot \sin(2\theta_{sp2} - \mu_2) - \frac{1}{2}(\hat{V}_{2,t} + \hat{V}_{2,r}) \cdot \sin(2\phi_b) \\ b_3 &= \frac{1}{2}(\hat{u}_2 + \hat{v}_2) \cdot \cos(2\theta_{sp2} - \mu_2) + \frac{1}{2}(\hat{V}_{2,t} + \hat{V}_{2,r}) \cdot \cos(2\phi_b)\end{aligned}\quad (10)$$

where $\theta_{sp2} = \cot \mu_2 \ln(R/R_{02})$ belongs to the bisymmetrical (mode $m = 2$) of the spiral perturbations. Eq. 10 shows that the spiral term at the coefficients a_1, b_1, a_3, b_3 is modulated by the periodic sine or cosine functions. The amplitudes of the tangential and radial components of the non-circular flow caused by the bar, $\hat{V}_{2,t}(R)$ and $\hat{V}_{2,r}(R)$, respectively, are both functions of the radius. Since the elliptical bar potential decreases monotonously with radius R the bar term in Eq. 10 also decreases monotonously. Eq. 2 and Eq. 8

correspond to the radial model by [Spekkens & Sellwood \(2007\)](#) with additional terms of spiral perturbations. Eq. 9 and Eq. 10 correspond to the bisymmetric model by the same authors with additional terms of spiral perturbations. We refer to the model described by Eq. 2 and Eq. 8 as the radial model with spiral perturbations and to the model described by Eq. 9 and Eq. 10 as the bisymmetric model with spiral perturbations.

In the outer part of the galaxy, the impact of the elliptical bar potential decreases quickly with radius R . A bar term would add to the radial symmetric (outflow/inflow) motion and the impact of the spiral term, or vanish. This means that beyond the bar Eq. 9 and Eq. 10 will coincide with Eq. 2 and Eq. 8. Since our main goal is a study of the impact of spirals on the spatial distribution of tracers, we adopt the radial model with spiral perturbations (Eq. 2 and Eq. 8) outside the bar. The pure radial outflow or inflow velocities contribute to the first Fourier harmonic (b_1) while the pitch angle μ_2 and characteristic radius R_{02} will be determined from the third Fourier harmonic. The radial disturbance by the bar has no impact on the definition of the geometrical parameters of the spiral arms.

3.2 Determination of the galaxy inclination and the position angle of the major axis

Here we estimate the galaxy inclination and the position angle of the major axis from the analysis of the observed velocity field and compare them with the values for the same quantities obtained from the analysis of the surface brightness distribution ([Zinchenko et al. 2016](#)). One may expect that the rotation makes a dominant contribution to the observed line-of-sight velocities. This means that the ratio of the Fourier coefficients b_1/a_1 is minimized if the galaxy inclination and position angle of the major axis are correct. It is expected that the velocities of the radially symmetric motions V_R are within $10 - 20 \text{ km s}^{-1}$, the velocities of the spiral perturbations δV_R within $5 - 10 \text{ km s}^{-1}$ ([Rohlf 1977](#)), and the rotation velocities V_θ within $150 - 300 \text{ km s}^{-1}$. Then the expected value of the ratio b_1/a_1 does not exceed $10\% - 15\%$ if the values of i and PA are correct. The radial velocities can reach unrealistically large values (which may be comparable to the rotation velocities or even exceed them) if the values of i and PA are not correct. Thus, PA and i are estimated from the requirement that the ratio of the Fourier coefficients b_1/a_1 is minimized for the correct values of i and PA .

We first consider a set of values of galaxy inclinations and position angles of the major axis with large steps, $\Delta i = 5^\circ$ and $\Delta P = 10^\circ$. A set of deprojected coordinates of individual pixels in the target galaxy for each set of the values of i and PA is obtained. Then a set of the coefficients $a_0, a_1, b_1, a_2, b_2, a_3$, and b_3 of Eq. (7) is determined for each set of the deprojected coordinates of the individual pixels by fitting to the line-of-sight velocities. The disc is divided into annuli of width $\Delta R = 1 \text{ kpc}$ in the plane of the target galaxy (see 3.5). The coefficients $a_0, a_1, b_1, a_2, b_2, a_3$, and b_3 are assumed to be equal for all the pixels within a given annulus. Assuming that the rotation makes a dominant contribution to the observed line-of-sight velocities we choose the values of i and PA that minimize the ratio of the Fourier coefficients b_1/a_1 as an approximation of the position angle of the major axis and the inclination angle of the galaxy. Fig. 4(a,b) shows the Fourier coefficient ratio b_1/a_1 as a function of PA and i for the galaxy NGC 36. To avoid crowding in the diagrams, the data are presented for the interval from 4.5 kpc to 14.5 kpc (from $0.20R_{25}$ to $0.65R_{25}$) with a step size of 2 kpc. Each curve corresponds to a single annulus. The step size in PA is $\Delta PA = 10^\circ$ and the step size in i is $\Delta i = 5^\circ$. Each ring zone shows a different b_1/a_1 value, but every curve has its minimum at the same

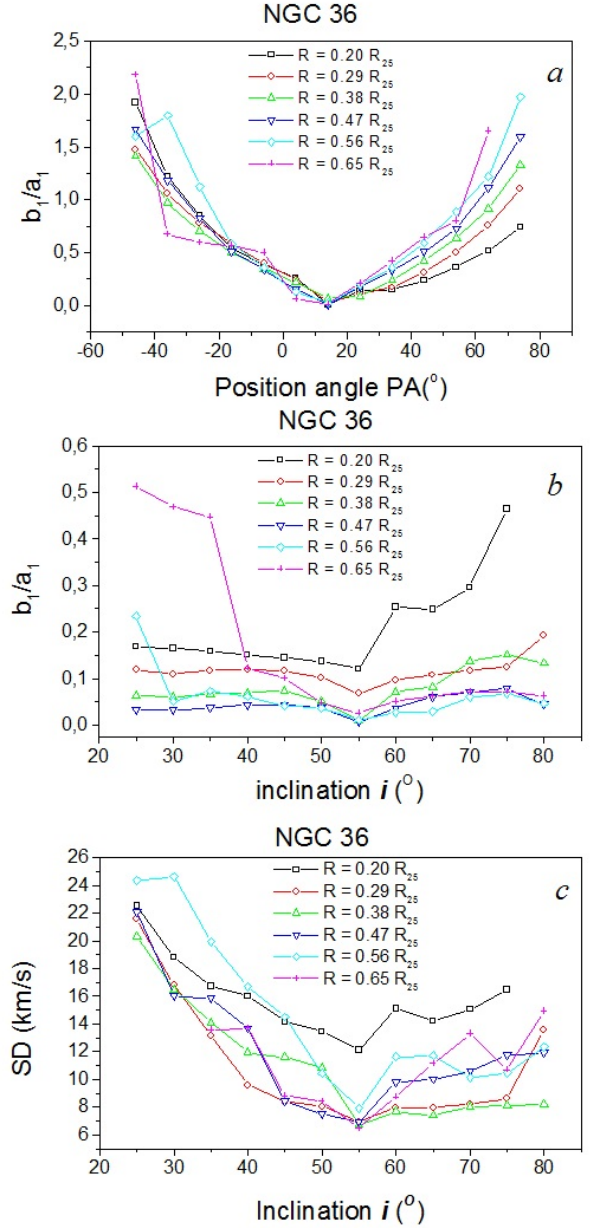


Figure 4. The change of the ratio of the Fourier coefficients b_1/a_1 in dependence on the proposed values of position angle PA (a) and inclination angle i (b) in NGC 36. c) The change of the standard deviation SD of the observed line-of-sight velocities from the predicted ones in dependence on the proposed values of the inclination angle i in NGC 36.

$PA = 14^\circ$ and at the same $i = 55^\circ$. In some zones the minimum of the curve in the b_1/a_1 vs. i diagram is not so prominent as in the b_1/a_1 vs. PA diagram. Therefore, we consider an additional diagram. Fig. 4(c) shows the standard deviation SD of the observed line-of-sight velocity in an annulus compared to the one predicted by Eq. 7 as a function of inclination angle i for NGC 36. The minimum value of the SD occurs at the same inclination $i = 55^\circ$ as in the previous b_1/a_1 vs. i diagram. Every annulus shows different SD values, but almost all curves have a similar minimum of $SD \approx (6-8) \text{ km s}^{-1}$ at the same $i = 55^\circ$.

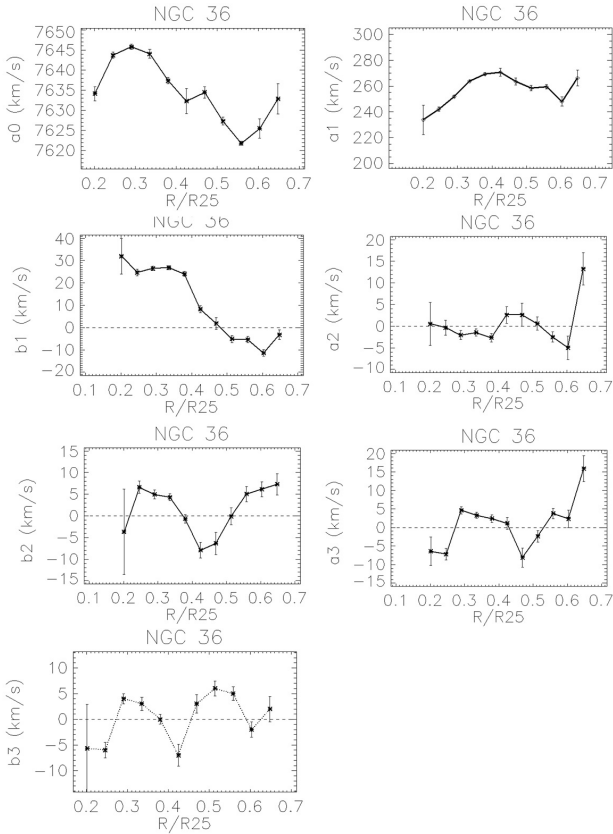


Figure 5. The radial change of the Fourier coefficients a_0 , a_1 , b_1 , b_2 , a_3 , and b_3 in NGC 36.

Next, we use a set of PA and i values with smaller step sizes of 2° to find more accurate values of the PA and i for the target galaxies. The obtained values of PA and i are listed in Table 3 (Columns 2 and 3, respectively) and are used below to find the deprojected coordinates of the spaxels with measured oxygen abundance and Balmer decrement.

Our obtained values of PA and i are generally in agreement with the photometry-based values of the PA and i reported in Table 1. The inclination of the galaxy NGC 36 determined here from the kinematics ($i = 55^\circ$) agrees with axis ratio $b/a = 0.56$ reported in the Uppsala General Catalogue of Galaxies (Nilsson 1973) and is close to the $b/a = 0.62$ given in the Third Reference Catalogue of Bright Galaxies (RC3 de Vaucouleurs et al 1991).

We only find a significant discrepancy between the values of the PA determined by the different methods for the galaxy NGC 7653: $PA = 140^\circ$ listed in the NED data base based on the angular diameters measured in K_s (2MASS “total”) passband, $PA = 172.5^\circ$ given in the LEDA data base, $PA = 175^\circ$ based on the photometry map of Zinchenko et al. (2016), and $PA = 165^\circ$ obtained here for the velocity map. It should be noted that NGC 7653 is a nearly face-on galaxy.

3.3 Determination of the systemic velocity of galaxies from the velocity map

The deprojected coordinates of each pixel in the target galaxy are determined with the position angle of the major axis and the galaxy inclination obtained in Subsection 3.2. The galactic disc

is divided into several annuli of a width of $\Delta R = 1$ kpc. For every annulus, we determine the seven unknown Fourier coefficients a_0 , a_1 , b_1 , a_2 , b_2 , a_3 , and b_3 of Eq. (7) using a least-squares method. The step size of $\Delta R = 1$ kpc provides 50 to 200 data points in each annulus in the interval of galactocentric distances from $R \sim 0.2R_{25}$ to $R \sim R = 0.7R_{25}$. Thus the number of data points (spaxels) in each annulus is large enough for a reliable determination of the coefficients of Eq. (7). The determinations of the coefficients a_0 , a_1 , b_1 , a_2 , b_2 , a_3 , and b_3 in a several annuli allows us to assess the radial change of these coefficients.

Fig. 5 shows an example of the radial change of the coefficients a_0 , a_1 , b_1 , a_2 , b_2 , a_3 , and b_3 in case of NGC 36. The range of galactocentric distances where the coefficients were determined covers a large part of the disc from approximately $R = 0.2R_{25}$ to $R = 0.7R_{25}$. As was noted in Subsection 3.1 the Fourier coefficients contain information on the systemic velocity of the galaxy, V_{gal} , the pure circular motion, $V_\theta(R)$, the radially symmetric motion, V_R , the peculiar velocities caused by the spiral arms, and the geometric shape of the arms.

First we estimate the systemic velocity V_{sys} of the galaxy, which is a projection of the velocity of the galaxy as a whole along the line-of-sight. As noted above (Section 3, Eq. 8), the zeroth Fourier coefficient a_0 includes contributions from the first mode of the spiral density wave and from the space velocity of the galaxy.

If the true value of the systemic velocity V_{sys} is subtracted from the line-of-sight velocity of each point (spaxel) then the coefficient a_0 expresses the impact of the spiral wave only and changes along the radius as a sine function

$$a_0 = \frac{1}{2}(\hat{u}_1 - \hat{v}_1) \cdot \sin(\cot \mu_1 \ln(R/R_{01}) + \mu_1). \quad (11)$$

The radially averaged value of a_0 must be close to zero, and the absolute value of maximum positive and negative amplitudes must be equal to each other. This condition can be used to estimate the true value of the systemic velocity V_{sys} . To do so, we constructed a set of diagrams of a_0 vs. R for different values of the V_{sys} . The value of the V_{sys} for which the absolute values of the maximum positive and negative values of the a_0 are equal to each other is adopted to be true. In this case, the absolute value of the a_0 corresponds to the amplitude of the non-circular perturbations caused by the spiral density wave.

Fig. 6 shows the value of a_0 obtained with the true V_{sys} as a function of galactocentric distance for each galaxy. We assume that Fig. 6 shows the radial change of the non-circular perturbation caused by the first mode ($m = 1$) of the spiral density wave in our target galaxies. The bars in Fig. 6 show the errors of the zeroth Fourier coefficients a_0 , determined from the standard least-squares procedure. The large number (50 – 200) of the conditional equations (because of the large number of measurements) in each annulus provides low uncertainties of a_0 , i.e., the errors are significantly lower than the amplitude of the non-circular perturbations caused by the spiral density wave. One can see from Fig. 6 that the amplitude of non-circular velocities is around 10 km s^{-1} , which agrees with the line-of-sight components of the density wave motions predicted by the model (see Fig. 12 in Rots (1975)). This fact can be considered as additional evidence in favor of the validity of the value of V_{sys} .

Our estimates of the systemic line-of-sight velocities V_{sys} agree with the values of other authors (listed in the NED database): $6224 \pm 12 \text{ km s}^{-1}$ for NGC 36 (Karachentsev & Makarov 1996), $5394 \pm 5 \text{ km s}^{-1}$ for NGC 180 (de Vaucouleurs et al 1991), 2944 ± 8

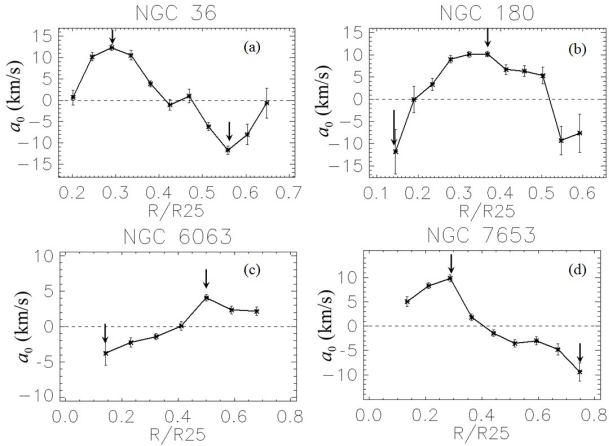


Figure 6. The coefficient a_0 , computed for the true V_{sys} , as a function of galactocentric distance in our target galaxies. The $a_0(R)$ illustrates the radial change of the non-circular perturbations of the velocity caused by the first mode ($m = 1$) of the spiral density wave (see Eq. 11). The arrows show the positions of the maximum positive and negative amplitudes of perturbations, caused by the spiral density wave.

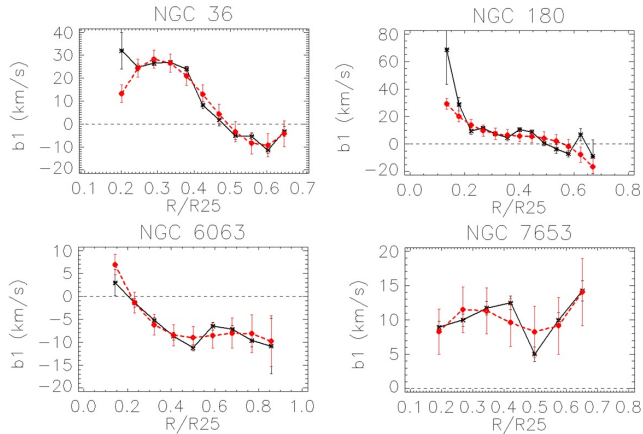


Figure 7. Fourier coefficient b_1 as a function of galactocentric distance in our target galaxies (black curve). The Fourier coefficient b_1 illustrates the radial change of non-circular perturbations of the velocity caused by the radially symmetric motion V_R and the second mode ($m = 2$) of the spiral density wave (see Eq. 8). The red curve is a model used to determine the radially symmetric motion V_R and the amplitude of the velocity perturbation caused by the second mode of the spiral density wave.

km s^{-1} for NGC 6063 (Fixsen et al. 1996), and $4378 \pm 20 \text{ km s}^{-1}$ for NGC 7653 (Mould et al. 2000).

The obtained values of the systemic velocities of the target galaxies are given in Column 4 of Table 3. The uncertainty of the systemic velocity V_{sys} is estimated as the sum of the error in the line-of-sight velocity and the maximum amplitude of the first mode.

3.4 Radially symmetric motions in the target galaxies obtained from velocity maps

The radially symmetric motion V_R can be determined from the radial change of the first Fourier harmonics (black curves in Fig. 7). Expression 3 of Eq. 8 shows that the radial motion V_R contributes

Table 2. Radially symmetric motion in our target galaxies.

Galaxy	V_R (km/s) ^a
NGC 36	9.1 ± 3.1
NGC 180	7.0 ± 3.4
NGC 6063	-4.6 ± 1.2
NGC 7653	10.1 ± 1.4

^a Since the side of the disk nearest to the observer disk along the minor axis is unknown, it is not possible to distinguish between inflow and outflow motion.

to the Fourier coefficient (b_1) and mixes with the velocity perturbation from the second mode $m = 2$ of the spiral density wave. First, we consider the barred galaxies NGC 36 and NGC 180. There are large radial velocities of $V_R > 30 \text{ km s}^{-1}$ (NGC 36) and $V_R > 60 \text{ km s}^{-1}$ (NGC 180) in the inner parts of both barred galaxies. We assume that this is an effect of the bar. The large error of coefficient b_1 in these points suggests that there is an explicit contribution of radial streaming velocities of the bar to the azimuthally averaged radial motion in NGC 36 and NGC 180.

Fig. 7 shows that there is a periodical component of the radial motion in the middle and outer parts of disc. The periodical component of the coefficient b_1 is shifted relative to the zero velocity line (dashed line in Fig. 7). This may be an effect of the large-scale radial outflow/inflow motion outside of the bar region. We approximated the radial change of the coefficient b_1 by a polynomial function of the third degree (red curve). As a sine or cosine shape of the variable term of the polynomial in barred galaxies corresponds rather to the spiral term than the bar term in Eq. 10, we made the simplest assumption that the variable term of the polynomial describes the impact of the spirals. The constant term may be explained as an azimuthally averaged radial outflow/inflow motion, while the impact of the bar term in the outer regions is negligible. This means that the coefficient $b_1(R)$ comprises generally the radial outflow/inflow motion V_R and the radial component of the velocity perturbations from spirals. The relative small errors of the coefficient b_1 in the outer regions of the barred galaxies NGC 36 and NGC 180 may indicate that a contribution of radial streaming velocities in the bar to the azimuthally averaged radially symmetric motion in NGC 36 and NGC 180 is small outside the bar. So we explain the radial change of the coefficient $b_1(R)$ with the help of the radial model with spiral perturbations (Eq. 8). The curve can be interpreted as follows. The Fourier coefficient b_1 comprises a constant radially symmetric large-scale component V_R and a periodical component of the non-circular motion caused by spiral perturbations outside the region with bar impact. Table 2 lists the radial velocities in our target galaxies. Similar radial velocities were detected in NGC 2976 by Spekkens & Sellwood (2007).

3.5 Determination of the geometrical parameters of spiral arms from the velocity map

Despite the observational fact that spiral arms in a real galaxy never have a strict geometric form because other local structures may muddle their appearance, investigators always try to describe the large-scale spiral structure of galaxies using a model of regular geometric form. To minimize the influence of local structures, a large radial interval should be analyzed. On the other hand, observations show that the pitch angle can vary along the radius (the change can exceed 20% (Savchenko & Reshetnikov 2013)). This suggests that

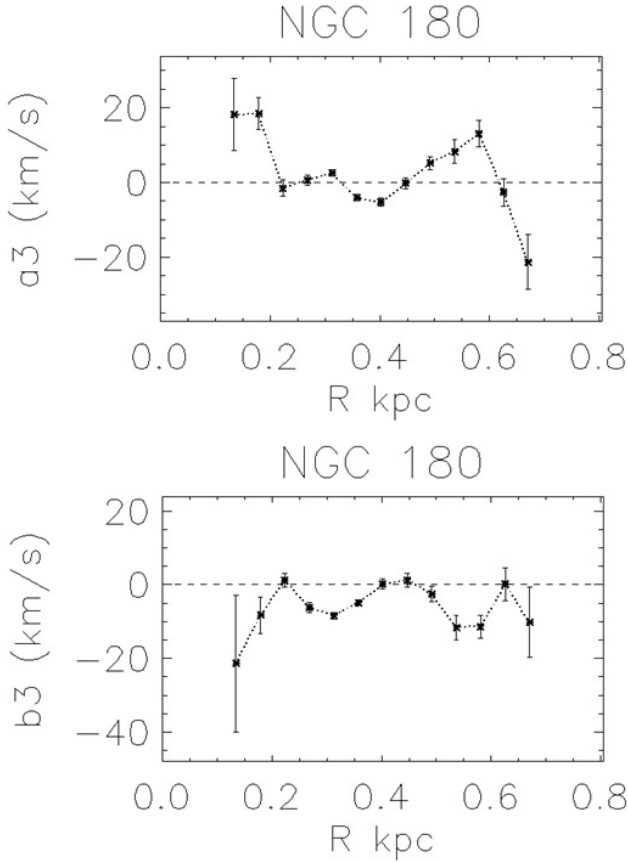


Figure 8. The radial change of the Fourier coefficients a_3 and b_3 in NGC 180 shows that starting at about $0.2R_{25}$, the periodic component associated with the spiral velocity perturbation dominates the monotonically decreasing component of the bar term in the coefficients a_3 and b_3 from equation Eq. 10.

a small radial interval should be analysed. Therefore the number of annuli used to determine the pitch angle is smaller than the total number of annuli adopted when the Fourier coefficients were computed.

In the current study, we adopt a logarithmic form of spiral arms because it appears suitable and leads to a satisfactory fit. We should note that the procedure of the determination of the Fourier coefficients does not assume that the spiral arms are logarithmic. In earlier work, spirals of different shapes were compared with observed spiral structures (Considere & Athanassoula 1982, and references therein). It was found (Considere & Athanassoula 1982) that the deviations of logarithmic and other shapes of spiral arms are smaller than the dispersion in the positions of H II regions or other arm tracers.

A logarithmic spiral is defined by the expression

$$R = R_0 e^{(\tan(\mu)\theta)} \quad (12)$$

where R and θ are polar coordinates in the plane of the galaxy, and μ is a pitch angle of the spiral arm.

The change of the coefficient a_0 , computed for the true V_{sys} , with galactocentric distance (see Fig. 6 and Eq. 11) provides a possibility to define graphically the pitch angle μ_1 of the spiral arm. The phase difference between the maximum positive and the maximum negative deviations from the (dashed) line of zero velocity

is equal to π . Fig. 6a shows that the maximum positive deviation takes place at a galactocentric distance $R_{max}/R_{25} = 0.31$ and the maximum negative deviation occurs at a galactocentric distance $R_{min}/R_{25} = 0.58$ (marked with arrows) for the galaxy NGC 36. This results in a pitch angle of

$$\mu_1 = \arctan\left(\frac{1}{\pi} \ln\left(\frac{R_{min}/R_{25}}{R_{max}/R_{25}}\right)\right) \approx 11^\circ$$

where R/R_{25} is a fractional radius (the galactocentric distance normalized to the disc's isophotal radius at 25 mag arcsec⁻²). The graphical determination of the places with a given phase difference, e.g., π , for other galaxies is an ambiguous task. Assuming that the curve is a periodic function we determine the maximum positive and maximum negative deviations from the condition that the phase difference is equal to π (marked with arrows in Fig. 6). We find a pitch angle $\mu_1 \approx 17^\circ$ for NGC 180, $\mu_1 \approx 22^\circ$ for NGC 6063, and $\mu_1 \approx 16^\circ$ for NGC 7653.

The geometrical parameters of two-armed spirals μ_2 and R_{02} can be found from the radial change of the Fourier coefficients $a_3(R)$ and $b_3(R)$ (see Eq. 8). The sixth and seventh expressions of Eq. 8 give

$$\frac{a_3}{\sqrt{a_3^2 + b_3^2}} = \sin\left(2 \cot \mu_2 \ln(R/R_{02}) - \mu_2\right) \quad (13)$$

Eq. (13) can be rewritten as a linear regression

$$y = A + Bx \quad (14)$$

with the notations

$$\begin{aligned} x &= \ln(R) \\ y &= \arcsin\left(\frac{a_3}{\sqrt{a_3^2 + b_3^2}}\right) \\ A &= \mu_2 - 2 \cot(\mu_2) \cdot \ln(R_{02}) \\ B &= 2 \cot(\mu_2) \end{aligned}$$

The estimation of the coefficients of the regression (14) provides the geometrical parameters of two-armed spirals, μ_2 and R_{02} . Table 3 (Col. 6) shows estimations of the pitch angle of μ_2 of the two-armed spirals μ_2 in our sample using velocity field perturbations.

We note the following: NGC 36 has a relatively short bar, $R_{bar} \approx 0.14R_{25}$. We determine the pitch angle μ_2 and characteristic radius R_{02} from the coefficients a_3 and b_3 computed in the annuli outside the bar. So our radial model with spiral perturbations (Eq. 2 and Eq. 8) is applied.

NGC 180 has a relatively long bar, $R_{bar} \approx 0.3R_{25}$. The coefficients a_3 and b_3 used in the determination of the pitch angle μ_2 and characteristic radius R_{02} were computed for a number of annuli, some of which lie at the end of bar (from $0.23R_{25}$ to $0.3R_{25}$) while the others are located outside the bar (from $0.3R_{25}$ to $0.4R_{25}$). Fig. 8 shows that starting at about $0.2R_{25}$, the periodic term associated with the spiral velocity perturbation in the expressions (Eq. 10) for the coefficients a_3 and b_3 dominates over the monotonically decreasing term associated with the bar.

The application of the radial model (Eq. 2 and Eq. 8) to the non-barred galaxies NGC 6063 and NGC 7653 works well.

Since the pitch angle can vary along the radius (the change can exceed 20% (Savchenko & Reshetnikov 2013)), a limited interval of galactocentric distances R was used in the determination of the pitch angle. This reduces the number of annuli, which lowers the

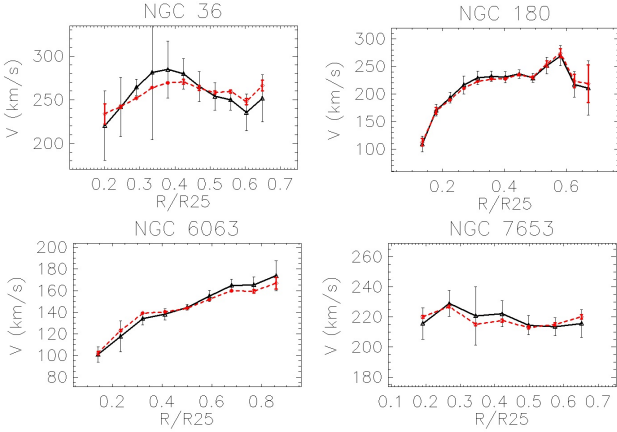


Figure 9. The rotation velocity $V_\theta(R)$ (solid black curve) and the value of the Fourier coefficient $a_1(R)$ (dotted red curve) as a function of galactocentric distance for the target galaxies.

accuracy of the pitch angle estimation. The intervals of galactocentric distances R used for each tracer are given in Columns 7, 9, and 11 of the Table 3. These intervals do not cover the whole disc.

3.6 Rotation curves of the target galaxies obtained from velocity maps

The Fourier coefficients $a_1(R)$ and $b_1(R)$ of Eq. (8) can be used to determine the rotation curve of a galaxy. The second expression of Eq. (8) can be rewritten as

$$V_\theta(R) = a_1(R) - \frac{1}{2}(\hat{u}_2 - \hat{v}_2) \cdot \sin(2 \cot \mu_2 \ln(R/R_{02}) - \mu_2). \quad (15)$$

The spiral perturbations in Eq. 15 are accounted for using the pitch angle μ_2 obtained in Sec. 3.5 and the amplitude derived from the Fourier coefficient b_1 . Neglecting the tangential bar term in the Eq. 8 affects the estimation of the average rotation velocity and can result in a significant error of the rotation curve in the inner annuli for the galaxy NGC 180 with its long bar. The rotation curve of the galaxy NGC 36 with a small bar is derived outside the bar region.

Fig. 9 shows the rotation velocity $V_\theta(R)$ (solid black curve) and the value of the Fourier coefficient $a_1(R)$ (dashed red curve) as a function of galactocentric distance for the galaxies considered. We note that the error bar in the a_1 coefficient is substantially smaller than the error bar in V_θ except for a few cases, such as the last point of the rotation curve in NGC 180, where the large error of a_1 corresponds to the large error of V_θ . Sources of large errors of rotation velocities $V_\theta(R)$ lie in the uncertainties of the pitch angle μ_2 caused by the complex structure of the spiral patterns and variations of the pitch angle with galactocentric distance, as well as in uncertainties of the radial and tangential disturbances caused by the bar in barred galaxies. A precise determination of the pure rotation curve remains a difficult task and depends on the applied method of the decomposition of the observed velocities.

4 SPIRAL ARMS TRACED BY ABUNDANCE AND EXTINCTION

Here we examine the manifestation of spiral arms in the oxygen abundance ($12 + \log(O/H)$) and Balmer decrement ($I_{H\alpha}/I_{H\beta}$) distributions across the discs of our galaxies. Since the high-density

(dust) clouds are concentrated along the spiral arms one can expect that the extinction is higher in the spiral arms than in the interarm regions. The star formation regions are also concentrated in the spiral arms. As consequence, the Type II supernova explosions responsible for the production and ejection of the bulk of oxygen into the interstellar gas occur more often in spiral arms than in the interarm regions. If the rate of the dissemination, dispersion, and mixing of the newly produced elements in the gas is slow enough then one can expect that there is an oxygen abundance enhancement in the spiral arms.

4.1 Determination of spiral arms from the abundance (extinction) map

We assume that the oxygen abundance distribution in the interarm regions of the disc, I_0 , is axisymmetric and that the enhancement of the oxygen abundance in the spiral arms, I_{sp} , is small in comparison to the oxygen abundance in the interarm region at a given galactocentric distance. Then the oxygen abundance distribution in the disc, I , is given by the expression

$$I(R, \theta) = I_0(R) + I_{sp}(R, \theta), \quad |I_{sp}| \ll |I_0|. \quad (16)$$

The distribution of the enhancement of the oxygen abundance across the spiral arms, I_{sp} , is assumed to be

$$I_{sp} = \hat{I} \cos \eta. \quad (17)$$

According to Eq. (17), the line of equal spiral arm phase $\eta = \text{const}$ is a line of equal enhancement of the oxygen abundance. It means that the centre of a spiral arm ($I_{sp} = \hat{I}$) is defined by the condition $\eta = 0$. The values of $\eta = \pm\pi/2$ correspond to the outer and inner spiral arm borders ($I_{sp} = 0$).

Taking into account Eq. (4) and Eq. (17) and grouping the sine and the cosine terms of identical quantities of θ , Eq. (16) can be rewritten in the form

$$I(R, \theta) = a_0 + a_1 \cos(\theta) + b_1 \sin(\theta) + a_2 \cos(2\theta) + b_2 \sin(2\theta) \quad (18)$$

where the coefficients $a_0(R)$, $a_1(R)$, $b_1(R)$, $a_2(R)$, and $b_2(R)$ are

$$\begin{aligned} a_0 &= I_0(R) \\ a_1 &= \hat{I}_1 \cos(\cot \mu_1 \ln(R/R_{01})) \\ b_1 &= \hat{I}_1 \sin(\cot \mu_1 \ln(R/R_{01})) \\ a_2 &= \hat{I}_2 \cos(2 \cot \mu_2 \ln(R/R_{02})) \\ b_2 &= \hat{I}_2 \sin(2 \cot \mu_2 \ln(R/R_{02})) \end{aligned} \quad (19)$$

The first mode $m = 1$ – one-armed asymmetric structure – contributes to the first Fourier harmonics of the azimuthal distribution of the abundance at a given galactocentric distance R . \hat{I}_1 is the maximum enhancement of the oxygen abundance in the centre of the one-armed spiral structure. The second mode $m = 2$ – a two-armed spiral – contributes to the quantities multiplied by the sines and the cosines of the polar angle 2θ ; i.e., to the second Fourier harmonics. \hat{I}_2 is the maximum enhancement of the oxygen abundance in the centre of the two-armed spiral structure. The coefficient $a_0(R) = I_0(R)$ is a function of the galactocentric distance R only and provides the radial abundance gradient in the interarm regions (see Fig 10).

The coefficients $a_0(R)$, $a_1(R)$, $b_1(R)$, $a_2(R)$, and $b_2(R)$ were obtained through the least-squares method using the abundance map $I(R, \theta)$ for each target galaxy.

Then we consider the radial change of the ratio

$$\frac{b_2}{\sqrt{a_2^2 + b_2^2}} = \sin(2 \cot \mu_2 \ln(R/R_{02})). \quad (20)$$

Table 3. The derived properties of our target galaxies (the position angle of the major axis, PA , the galaxy inclination angle, i , the systemic velocity, V_{gal} , the maximum rotation velocity, V_{max} , the pitch angle of the spiral arms, μ_2 , and the scaling factor R_{02}).

Galaxy	PA^a	i^a	V_{sys}	V_{max}	μ_2^b	ΔR^b	μ_2^c	ΔR^c	μ_2^d	ΔR^d	R_{02}
	deg	deg	km/s	km/s	deg	(R/R_{25})	deg	(R/R_{25})	deg	(R/R_{25})	(R/R_{25})
1	2	3	4	5	6	7	8	9	10	11	12
NGC 36	14	55	6253±29	279	10	0.29 - 0.44	11	0.45 - 0.67	11	0.45 - 0.67	0.53 ± 0.09
NGC 180	165	46	5405±14	277	18	0.23 - 0.37	17	0.24 - 0.38	18	0.23 - 0.45	0.29 ± 0.06
NGC 6063	156	58	2945±11	168	23	0.34 - 0.48	24	0.54 - 0.85	22	0.36 - 0.63	0.57 ± 0.15
NGC 7653	165	31	4356±21	225	14	0.52 - 0.65	15	0.31 - 0.47	12	0.31 - 0.44	0.43 ± 0.19

^(a)Uncertainties of the determination of PA and i are $\pm 2^\circ$.

^(b)Value estimated from the velocity field.

^(c)Value determined from the extinction map ratio $I_{Ha}/I_{H\beta}$.

^(d)Value is obtained from the oxygen abundance map.

The step size intervals of the galactocentric distances ΔR used for the determination of the pitch angle of the spiral arms with different tracers are given in Columns 7, 9, and 11.

With the definitions

$$x = \ln(R)$$

$$y = \frac{1}{2} \arcsin\left(\frac{b_2}{\sqrt{a_2^2 + b_2^2}}\right)$$

$$A = -\cot(\mu_2) \cdot \ln(R_{02})$$

$$B = \cot(\mu_2)$$

Eq. (20) can be rewritten as a linear regression (Eq. (14)). The coefficients A and B of the linear regression are obtained through the least-squares method. The pitch angle of a two-armed spiral, μ_2 , and the constant R_{02} are then defined by the obtained coefficients A and B . Our results are presented in Table 3 (Column 10).

This method can be applied not only to the abundance maps, but to any scalar field distributed across a galactic disc. In this study we also apply it to the determination of spiral arms from the extinction maps (Column 8 in Table 3).

4.2 Metallicity gradients in discs and parameters of spiral arms derived from abundance maps

We noted above that the coefficient $a_0(R) = I_0(R)$ gives the radial abundance gradient in the interarm regions. Fig 10 shows the obtained radial oxygen abundance gradients in the interarm regions in our four galaxies. The traditional form of the abundance gradient (linear regression) is adopted:

$$12 + \log(O/H) = 12 + \log(O/H)_0 + grad \cdot (R/R_{25}) \quad (21)$$

where $12 + \log(O/H)_0$ is the extrapolated central oxygen abundance and the $grad$ is the slope of the oxygen abundance gradient expressed in terms of dex R_{25}^{-1} . The R/R_{25} is the fractional radius (the galactocentric distance normalized to the disc isophotal radius, R_{25}).

The obtained central oxygen abundance and the slope of the oxygen abundance gradient in the interarm regions of our galaxies are listed in Table 4 and shown in Fig. 10. The slopes of the metallicity gradients expressed in terms of dex R_{eff}^{-1} are also obtained using the values of the R_{eff} from Sánchez et al. (2014) (Table 4).

Fig 11 shows the enhancement of the oxygen abundance in the spiral arms as compared to the mean (azimuthally averaged) abundance in the interarm regions at a given galactocentric distance

Table 4. The extrapolated central oxygen abundance and the slope of the oxygen abundance gradient

Galaxy	$12 + \log(O/H)_0$	$grad_{dex/R_{25}}$	$grad_{dex/R_{eff}}$	R_{25}/R_{eff}
1	2	3	4	5
NGC 36	8.61 ± 0.01	-0.10 ± 0.02	-0.07	1.53
NGC 180	8.63 ± 0.01	-0.16 ± 0.02	-0.09	1.77
NGC 6063	8.573 ± 0.002	-0.189 ± 0.005	-0.09	2.02
NGC 7653	8.614 ± 0.001	-0.196 ± 0.003	-0.09	2.15

as a function of galactocentric distance for the galaxies considered. The enhancement caused by the second mode ($m = 2$) of the spiral density waves is considered. Inspection of Fig 11 shows that the enhancement of the oxygen abundance in the spiral arms is small and increases outwards from ~ 2 to ~ 8 per cent.

The comparison between the parameters of the radial distributions of the oxygen abundance in the interarm regions (the extrapolated central oxygen abundance and the slope of the oxygen abundance gradient) listed in Table 4 and the parameters of the radial abundance distribution for the whole discs (spiral arms and interarm regions) reported in Zinchenko et al. (2016) shows that these two sets of values are close to each other. This suggests that the influence of the spiral arms on the radial abundance gradient in galactic discs is small.

It should be noted that the location of the spiral arms can be established from the abundance map not for the whole disc but only for some range of galactocentric distances. These ranges are given in Table 3 (Column 11). The spiral arms start at some distance from the center and therefore the innermost part of the galaxies is excluded from our considerations. The spiral arms at the peripheral outer regions of our galaxies cannot be established because of the poor statistics of the observed points.

4.3 Spiral arms in our galaxies derived from extinction maps

The method described above and used for the analysis of the abundance map to trace the spiral arms can be also applied to the extinction map. Here we search for spiral arms in our target galaxies

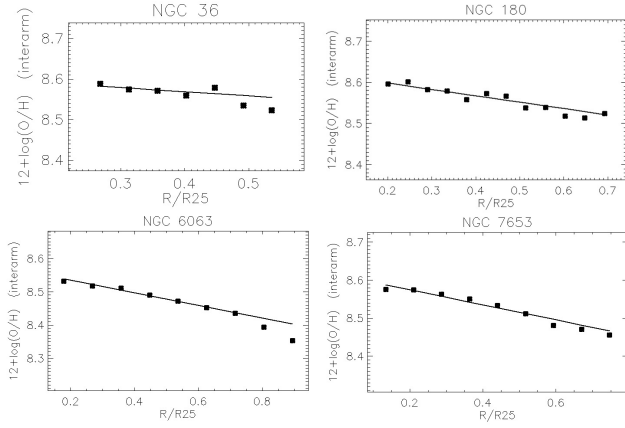


Figure 10. Radial abundance gradients in the interarm regions for our target galaxies. The squares stand for the oxygen abundances at different radii. The line shows the best fit to those data.

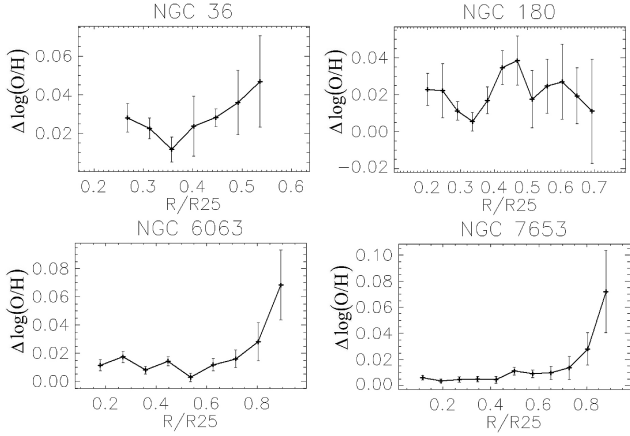


Figure 11. The enhancement of the oxygen abundance $\Delta \log(\text{O}/\text{H})$ in the spiral arms as compared to the interarm regions as a function of galactocentric distance for the target galaxies.

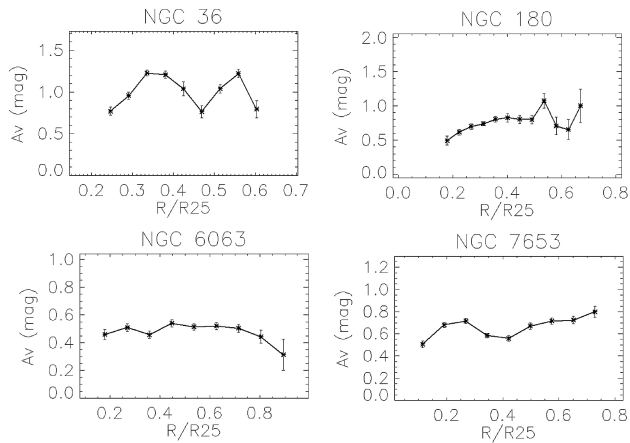


Figure 12. The visual extinction A_V as a function of galactocentric distance in our target galaxies. The points mark the azimuthally averaged values of extinction. The error bars show the scatter.

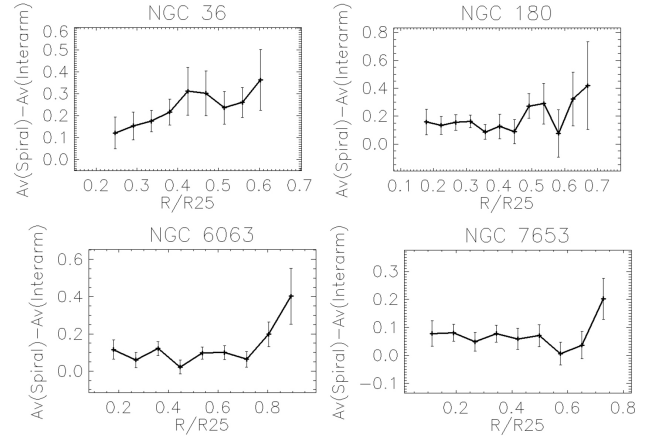


Figure 13. The difference between the total visual extinction in the spiral arms, $A_V(\text{Spiral})$, and the mean extinction in the interarm regions, $A_V(\text{Interarm})$, as a function of galactocentric distance.

using the Balmer decrement and succeeded in uncovering the spiral arms in each target galaxy.

Fig 12 shows the azimuthally averaged value of the visual extinction A_V in the interarm regions as a function of galactocentric distance in our target galaxies. Inspection of Fig 12 shows that there is no common systematic change of the extinction along the radial extent of the disc; instead the extinction is constant within the uncertainties.

Fig 13 shows the difference between the extinction in the spiral arms, $A_V(\text{Spiral})$, and the mean extinction in the interarm regions, $A_V(\text{Interarm})$, as a function of galactocentric distance. The difference $A_V(\text{Spiral}) - A_V(\text{Interarm})$ increases monotonically outwards.

5 DISCUSSION

Fig. 14 shows the spiral arms obtained from the maps of different tracers in the target galaxies. The spiral arms in Fig. 14 are shown within the range of galactocentric distances where they were detected (see Table 3).

Inspection of Fig. 14 (compare also the values of the pitch angle listed in Columns 6, 8, and 10 of Table 3) shows that the parameters of the spiral arms derived from maps of different tracers are in good agreement with each other. This is not surprising because of all three tracers are associated with ionized gas clouds. Since the high-density (dust) clouds are concentrated in the spiral arms one may expect a higher extinction in the spiral arms than in the interarm regions. The type II supernovae responsible for the oxygen enrichment of the interstellar gas are more often located in the spiral arms than in the interarm regions. Thus the spiral arms derived from the maps of different tracers are in line with the gravitational density wave nature of the spiral arms and the theory of the star formation. A similar conclusion has been reached by Sánchez-Menguiano et al. (2016b) on the base of the analysis of the VLT/MUSE data of the galaxy NGC 6754.

The reliability and accuracy of the parameters of the spiral arms obtained for each tracer is rather low because of the small amplitude of the disturbance of the tracer caused by the spiral arms and the relatively low spatial resolution of the observations. Moreover, a detailed photometric study and measurements of spiral arm pitch

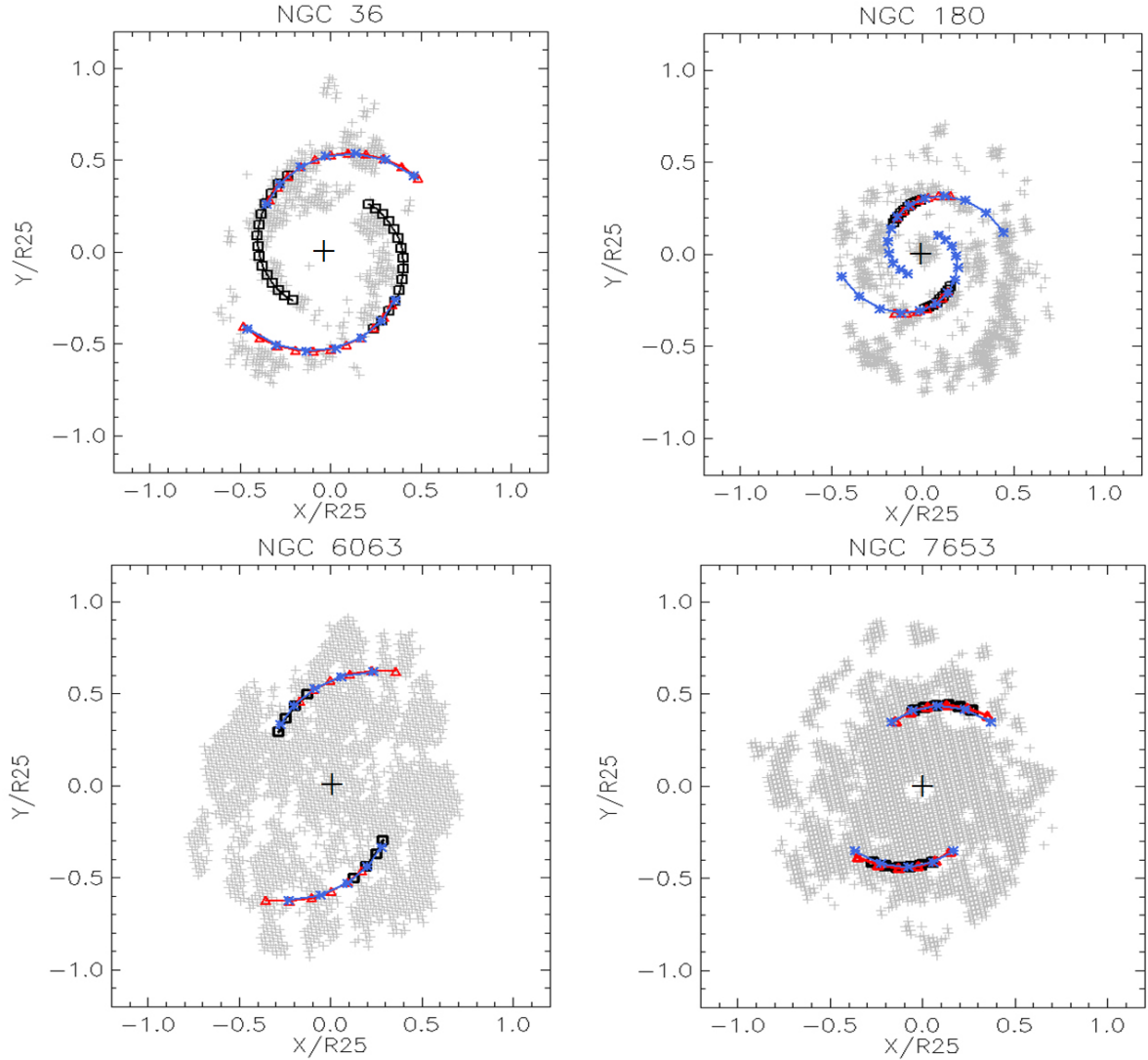


Figure 14. Comparison between spiral arms derived from the analysis of the velocity map (black squares), the extinction map (red triangles), and the oxygen abundance map (blue stars). The small grey plus signs mark the areas (pixels) with measured oxygen abundances. The large dark plus sign marks the position of the centre of the galaxy. Red rectangle shows the orientation and size of the bar in NGC 36 and NGC 180 (upper panels)

angles in 50 grand-design spiral galaxies (Savchenko & Reshetnikov 2013) shows that about 2/3 of these galaxies demonstrate pitch angle variations exceeding 20 per cent. This also influences the accuracy of the definition of pitch angles. The fact that the parameters of the spiral arms derived from the maps of our different tracers are close to each other supports the reliability of the obtained geometrical parameters of the spiral patterns.

Sánchez-Blázquez et al. (2014) noted that the non-linear coupling between the bar and the spiral arms is an efficient mechanism for producing radial migrations across significant distances within discs. The process of radial migration should flatten the stellar metallicity gradient with time and, therefore, one can expect flatter stellar metallicity gradients in barred galaxies. It is interesting to note that the metallicity gradients expressed in terms of dex R_{25}^{-1} in the barred galaxies NGC 36 and NGC 180 are flatter than in the unbarred galaxies NGC 6063 and NGC 7653. However, if the gradient is expressed in terms of dex R_{eff}^{-1} , then there is no difference between the gradients in barred and unbarred galaxies (Table 4). This agrees with the conclusion of Sánchez et al. (2014) and Sánchez-Blázquez

et al. (2014) that there is no difference in the slope of the metallicity gradients expressed in terms of dex R_{eff}^{-1} between barred and unbarred galaxies.

We found that the early-type spiral galaxies (NGC 36 and NGC 7653) demonstrate more tightly wound arms in comparison with the late-type spiral galaxies (NGC 180 and NGC 6063) as one would expect based on their morphological types. This is in agreement with previous results (e.g., Kennicutt 1981; Savchenko & Reshetnikov 2013).

It should be noted that Vogt et al. (2017) detected the presence of rapid abundance variations in the spiral galaxy HCG 91c based on the Multi Unit Spectroscopic Explorer (MUSE) observations. These variations can be separated in two distinct types, namely sub-kpc-scale variations associated with individual star-forming regions and kpc-scale variations correlated with the spiral structure of the galaxy. The authors conclude that the kpc-scale variations thus provide observational evidence that ISM enrichment is preferentially occurring along the spiral structure of HCG 91c, and less easily across the spiral arms.

It is known that the maximum rotation velocity, V_{\max} , of disc galaxies correlates with the absolute blue magnitude of the galaxy M_B and its morphological type (Rubin et al. 1980, 1982; Rubin 1983; Burstein & Rubin 1985). The values of the maximum rotation velocity V_{\max} derived in our current study (Column 5 in Table 3) are in agreement with the characteristic maximum rotation velocities for the galaxies of similar luminosity and morphological type.

We discussed in Sec. 3.6 a possible impact of the bar on the determination of the rotation curve $V_\theta(R)$. Through the analysis of the Fourier coefficient b_1 we found large radial velocities $V_R \approx (30\text{--}60)$ km s⁻¹ in the inner parts of both barred galaxies, while in outer part of the galaxies the radially symmetric large-scale motion is lower; $V_R \approx 10$ km s⁻¹.

The position angles of the major axis of a galaxy obtained here from the velocity field agree with the position angles determined from the analysis of the surface brightness distributions in Zinchenko et al. (2016). That is in line with the result of Barrera-Ballesteros et al. (2014), who did not find statistically significant differences between the kinematic PA and the global photometric orientation of the galaxy, including barred and unbarred objects.

Fig. 6 shows a variation of the zeroth coefficient a_0 with increasing galactocentric distance in our target galaxies (the true systemic velocity is subtracted from the measured velocity of each spaxel). Such a dependence of the zeroth coefficient on the galactocentric distance was also detected by Carignan et al. (1990) in the spiral galaxy NGC 6946 and by Sakhibov & Smirnov (2004) in NGC 628. Carignan et al. (1990) assumed that the coefficient a_0 comprises just the systemic velocity of the galaxy as a whole, V_{gal} , and explained the radial dependence of the zeroth coefficient by the periodic variation of the inclination of the galaxy disc from $i = 33^\circ$ up to $i = 43^\circ$. Sakhibov & Smirnov (2004) suggested that the radial dependence of the zeroth coefficient a_0 in NGC 628 can be explained with the first mode of a density wave, which makes a contribution in zeroth harmonics. The superposition of the first and second modes can result in asymmetric spiral structure, which is apparent in the maps of the metallicity distribution of NGC 180 and NGC 7653 (Fig. 14).

Sánchez et al. (2015) and Sánchez-Menguiano et al. (2016b) considered the azimuthal distribution of the residuals of the oxygen abundance for the individual H II regions in the galaxy NGC 6754 after subtracting the average radial gradient. They noted that the strongest residuals correspond to the spiral arms. The mean absolute value of the strongest residuals is below ~ 0.05 dex and changes with galactocentric distance. We found a similar picture for the enhancements of the oxygen abundance in the spiral arms as shown in Fig. 11.

Sánchez-Menguiano et al. (2017) carried out a study of the arm and interarm abundance distributions in a sample of 63 CALIFA spiral galaxies. They found that the differences between the gas abundances of spiral arms and interarm regions are small and statistically significant only for flocculent and barred galaxies. The small values of the enhancement of the oxygen abundance in the spiral arms obtained here for four galaxies is in agreement with their results.

6 CONCLUSIONS

We constructed maps of the observed velocity of the ionized gas, the oxygen abundance, and the extinction (Balmer decrement) in the discs of the four spiral galaxies NGC 36, NGC 180, NGC 6063,

and NGC 7653 based on integral field spectroscopy obtained by the Calar Alto Legacy Integral Field Area (CALIFA) survey. The maps were used to search for spiral arms in the discs of these galaxies via Fourier analysis. We considered non-circular motions, the enhancement of the oxygen abundance, and increased extinction as tracers of spiral arms.

The parameters of the spiral structure were obtained in all four galaxies considered and for each tracer. The pitch angles of the spiral arms obtained from the different tracers are close to each other. This strengthens the reliability of the obtained geometrical parameters of the spiral patterns although the accuracy of determination of these parameters for each tracer separately is low. The systemic velocity, inclination, position angle of the major axis, and rotation curve were also obtained for each target galaxy using the Fourier analysis of the two-dimensional velocity map.

The enhancement of the oxygen abundance in the spiral arms as compared to the abundance in the interarm regions at a given galactocentric distance is small, within a few per cent. This evidences that the influence of the spiral arms on the present-day radial abundance gradient in the discs of spiral galaxies is small and can be neglected in many tasks. There is no regular change of the extinction with galactocentric distance in the studied galaxies.

ACKNOWLEDGMENTS

We are very grateful to the referee for his/her constructive comments and recommendations, which significantly improved the article.

I. A. Z., L. S. P., E. K. G., and A. J. acknowledge support within the framework of Sonderforschungsbereich SFB 881 on “The Milky Way System” (especially via subprojects A5 and A6). SFB 881 is funded by the German Research Foundation (DFG).

I. A. Z. and L. S. P. and thank for the hospitality of the Astronomisches Rechen-Institut at Heidelberg University, where part of this investigation was carried out.

I. A. Z. acknowledges the support of the Volkswagen Foundation under the Trilateral Partnerships grant No. 90411.

This study uses data provided by the Calar Alto Legacy Integral Field Area (CALIFA) survey (<http://califa.caha.es/>). Based on observations collected at the Centro Astronómico Hispano Alemán (CAHA) at Calar Alto, operated jointly by the Max-Planck-Institut für Astronomie and the Instituto de Astrofísica de Andalucía (CSIC).

The authors acknowledge the usage of the HyperLeda data base (<http://leda.univ-lyon1.fr/>), the NASA/IPAC Extragalactic Database (<http://ned.ipac.caltech.edu>).

REFERENCES

- Asari N. V., Cid Fernandes R., Stasińska G., Torres-Papaqui J. P., Mateus A., Sodré L., Schoenell W., Gomes J. M., 2007, *MNRAS*, 381, 263
- Barrera-Ballesteros J. K., et al., 2014, *A&A*, 568, A70
- Barrera-Ballesteros J. K., et al., 2015, *A&A*, 582, 21
- Barnes E. I., Sellwood J. A., 2003, *AJ*, 125, 1164
- Bosma A., 1978, PhD, thesis, Univ. Groningen
- Bruzual G., Charlot S., 2003, *MNRAS*, 344, 1000
- Burstein D., Rubin V. C., 1985, *ApJ*, 297, 423
- Canzian B., 1993, *ApJ*, 414, 487
- Cardelli J. A., Clayton G. C., Mathis J. S., 1989, *ApJ*, 345, 245
- Carignan C., Charbonneau P., Boulanger F., Viallefond F., 1990, *A&A*, 234, 43

- Cid Fernandes R., Mateus A., Sodré L., Stasińska G., Gomes J. M., 2005, *MNRAS*, 358, 363
- Considera S., Athanassoula E., 1982, *A&A*, 111, 28
- Considera S., Athanassoula E., 1988, *A&AS*, 76, 365
- Elmegreen D. M., Elmegreen B. G., 1984, *ApJS*, 54, 127
- Eskridge P. B., et al., 2002, *ApJS*, 143, 73
- Fixsen D. J., et al., 1996, *ApJ*, 473, 576
- Fraternali F., Oosterloo T., Sancisi R., van Moorsel G., 2001, *ApJ*, 562, L47
- Fridman A. M., et al., 2001a, *MNRAS*, 323, 651
- Fridman A. M., Khoruzhii O. V., Lyakhovich V. V., Sil'chenko O.K., Zasov A.V., Afanasiev V.L., Dodonov S.N., Boulesteix J., 2001b, *A&A*, 371, 538
- Frick P., Stepanov R., Beck R., Sokoloff D., Shukurov A., Ehle M., Lundgren A. 2015, *A&A*, 585, 21
- García-Benito R., et al., 2015, *A&A*, 576, A135
- García-Lorenzo B., et al., 2015, *A&A*, 573, 59
- González Delgado R. M., et al., 2014, *A&A*, 562, A47
- González Delgado R. M., et al., 2016, *A&A*, 590, A44
- Grosbøl P. J., Block D. L., Patsis P. A., 1999, *Ap&SS*, 269, 423
- Holmes L., et al., 2015, *MNRAS*, 451, 4397
- Husemann B., et al., 2013, *A&A*, 549, A87
- Iye M., Okamura S., Hamabe M., Watanabe M., 1982, *ApJ*, 256, 103
- Izotov Y. I., Thuan T. X., Lipovetsky V. A., 1994, *ApJ*, 435, 647
- Kalnajs A. J., 1975, in Weliachew L., ed, *Colloques Internationaux du Centre National de la Recherche Scientifique No. 241, La Dynamique des galaxies spirales*. Editions du Centre National de la Recherche Scientifique, Paris, p. 103
- Karachentsev I. D., Makarov D. A., 1996, *AJ*, 111, 794
- Kennicutt R. C. Jr., 1981, *AJ*, 86, 1847
- Lin C. C., Yuan C., Shu F. H., 1969, *ApJ*, 155, 721
- Martín-Navarro I., et al., 2015, *ApJ*, 806, L31
- Mateus A., Sodré L., Cid Fernandes R., Stasińska G., Schoenell W., Gomes J. M., 2006, *MNRAS*, 370, 721
- Mould J. R., Huchra J. P., Freedman W. L. et al., 2000, *ApJ*, 529, 786
- Nilson R., 1973, *Acta Universitatis Upsalienis, Nova Regiae Societatis Upsaliensis, Series V: A Vol. 1*
- Osterbrock D.E., 1989, *Astrophysics of gaseous nebulae and active galactic nuclei*. University Science Books, Mill Valley, CA
- Paturel G., Petit C., Prugniel Ph., Theureau, G., Rousseau J., Brouty M., Dubois P., Chambrésy L., 2003, *A&A*, 412, 45
- Pérez E., et al., 2013, *ApJL*, 764, L1
- Pilyugin L. S., Grebel E. K., Mattsson L., 2012, *MNRAS*, 424, 2316
- Pilyugin L. S., Grebel E. K., Kniazev A. Y., 2014, *MNRAS*, 447, 131
- Rohlf K., 1977, *Lectures on density wave theory*. Lecture Notes in Physics Vol. 69, Springer Verlag, Berlin
- Rots A. H., 1975, *A&A*, 45, 43
- Rubin V. C., Burstein D., Thonnard N. 1980, *ApJL*, 242, L149
- Rubin V. C., Ford W. K. Jr., Thonnard N., Burstein D., 1980, *ApJ*, 261, 439
- Rubin V. C., 1983, in Athanassoula E., ed, *Proc. IAU Symp. 100, Internal kinematics and dynamics of galaxies*. D. Reidel Publishing Co., Dordrecht, p. 3
- Sakhibov F. K., Smirnov M. A., 1987, *SvA*, 31, 132
- Sakhibov F. K., Smirnov M. A., 1989, *SvA*, 33, 476
- Sakhibov F. K., Smirnov M. A., 1990, *SvA*, 34, 347
- Sakhibov F. K., Smirnov M. A., 2004, *Astronomy Reports*, 48, 995
- Sánchez S. F., et al., 2012a, *A&A*, 538, A8
- Sánchez S. F., et al., 2012b, *A&A*, 546, A2
- Sánchez S. F., et al., 2014, *A&A*, 563, A49
- Sánchez S. F., et al., 2015, *A&A*, 573, A105
- Sánchez-Blázquez P., 2014, *A&A*, 570, A6
- Sánchez-Menguiano L., 2016a, *A&A*, 587, A70
- Sánchez-Menguiano L., et al., 2016b, *ApJ*, 830, 40
- Sánchez-Menguiano L., et al., 2017, *A&A*, 603, 113
- Savchenko S. S., Reshetnikov V. P., 2013, *MNRAS*, 436, 1074
- Schinnerer E., Eckart A., Tacconi L. J., Genzel R., 2000, *AJ*, 533, 850
- Spekkens K., Sellwood J. A., 2007, *ApJ*, 664, 204
- Vallée J. P., 1995, *ApJ*, 454, 119
- de Vaucouleurs G., de Vaucouleurs A., Corwin H. G., Buta R. J., Paturel G., Fouque P. Third Reference Catalogue of Bright Galaxies (RC3), 1991, Springer-Verlag, New York
- Visser H. C. D., 1980, *A&A*, 88, 149
- Vogt F. P. A., Pérez E., Dopita M. A., Verdes-Montenegro L., Borthakur S., 2017, *A&A*, 601, A61
- Walcher C. J., et al., 2014, *A&A*, 569, A1
- Zinchenko I. A., Pilyugin L. S., Grebel E. K., Sánchez S. F., Vilchez J. M., 2016, *MNRAS*, 462, 2715